

Phase Equilibria of CO₂ and *n*-Alkanes in Bulk and Confined Space Using Parallelized Wang-Landau Transition-Matrix Monte Carlo Simulations

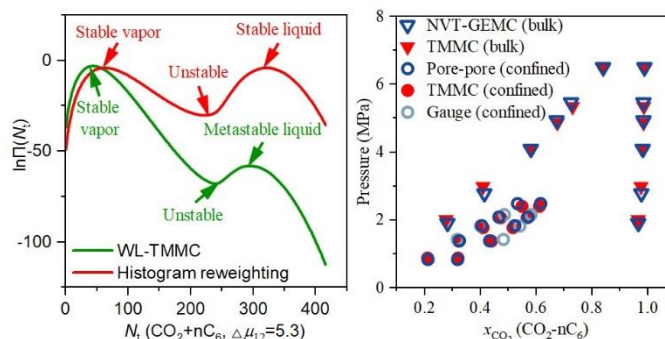
Jilong Xu^a, Harold W. Hatch^b, Vincent K. Shen^b, Zhehui Jin^{a*}

^a School of Mining and Petroleum Engineering, Department of Civil and Environmental Engineering, University of Alberta, Edmonton, Alberta T6G 1H9, Canada

^b Chemical Informatics Research Group, Chemical Sciences Division, National Institute of Standards and Technology, Gaithersburg, Maryland 20899-8380, United States

(Dated: April 1, 2025)

Abstract: The accurate and fast simulation of CO₂ and *n*-alkane phase equilibria is crucial for guiding their industrial applications. We used Wang-Landau Transition-Matrix Monte Carlo (WL-TMMC) with the Free Energy and Advanced Sampling Simulation Toolkit (FEASST) software to compute the vapor-liquid equilibrium (VLE) of CO₂-methane and CO₂-hexane systems in both bulk and confined spaces. The bulk-phase simulation results were compared with literature data and constant volume Gibbs Ensemble (NVT-GEMC) results, with relative errors less than 6%. For confined systems, the results were compared with gauge cell grand-canonical Monte Carlo (gauge-GCMC) and pore-pore GEMC, with relative errors less than 8%. Notably, the WL-TMMC exhibits significant advantages in computing VLE for confined spaces. It requires only a single simulation to determine a pair of VLE points without being constrained by prespecified chemical potentials or pore geometry. Furthermore, the method provides free energy information for different fluid states, enabling the construction of a complete van der Waals loop from a single simulation. In conclusion, we demonstrate that WL-TMMC in FEASST is a robust and reliable tool for studying CO₂-*n*-alkane VLE.



(This is an author reprint of <https://doi.org/10.1021/acs.energyfuels.5c00420>)

1. INTRODUCTION

The phase behavior of CO₂-hydrocarbon mixtures is important in various engineering applications, including enhanced oil recovery,^{1,2} CO₂ storage,^{3,4} and propulsion system design.⁵ In the petroleum industry, injecting CO₂ into reservoirs for fracturing and displacing fluids has emerged as a promising approach, as it can enhance oil/gas recovery while sequestering CO₂.⁶ During these processes, CO₂ can either separate from hydrocarbons as bubbles^{7,8} or remain miscible with them.⁹ When injected into subsurface nanoporous media (such as shale/tight formations), the strong solid-liquid interactions within nanopores¹⁰ further complicate the phase behavior of their mixtures.¹¹ Given that *n*-alkanes are the primary components of hydrocarbons,^{12,13} studying the phase equilibria of CO₂ and *n*-alkanes in both bulk and confined spaces is crucial.

Based on the accurate description of microscopic interactions, Monte Carlo (MC) simulations have become a powerful tool for studying phase equilibria in both bulk and confined systems. These simulations serve as an important complement to experimental work and offer critical validation data for theoretical models. Since being introduced by Panagiotopoulos et al.,^{14,15} the Gibbs

*E-mail: zhehui2@ualberta.ca

Ensemble Monte Carlo (GEMC) method has become one of the most widely-used methods for simulating phase equilibria of pure component and multicomponent fluids in bulk systems. It employs multiple simulation boxes to explicitly model different phases without the need to specify chemical potentials in advance. Later, Panagiotopoulos et al.¹⁶ proposed the pore-pore GEMC method to simulate phase equilibria in confined spaces. However, this method requires shifting the pore volume, which is difficult to practically achieve for irregular pores. Additionally, when applied to nanopores with strong fluid-surface interactions, the determined coexistence points are highly sensitive to initial configurations.¹⁷ Therefore, it is necessary to perform additional simulations in advance to determine the initial configuration.^{18,19} Another effective modified GEMC method for confined fluids is the gauge cell method. The gauge-GEMC^{17,20} uses small gauge boxes to equilibrate the confined system. Due to the limited capacity of gauge boxes, the fluid in the confined box can exist in stable, metastable, and unstable states. Therefore, a van der Waals (vdW) loop can be constructed to determine the vapor-liquid equilibria (VLE). However, this method is primarily used for studying the VLE of pure fluids,²¹⁻²³ which becomes computationally expensive for

multicomponent systems. Subsequently, the μVT gauge-GEMC, also known as the gauge cell grand-canonical MC (gauge-GCMC), was proposed for multicomponent systems,²⁴ which has been used to study the binary and ternary equilibria of n -alkanes²⁴ and the binary equilibria of CO₂- n -alkane systems under confinement.²⁵ However, constructing each vdW loop and determining the corresponding VLE points require at least a dozen simulations, which increases the computational cost of gauge-GCMC. GCMC is a method proposed earlier than GEMC, which simulates a system by connecting the simulation box to an implicit infinitely-large reservoir, operating at a given chemical potential (μ), volume (V), and temperature (T). Traditional GCMC gradually adjusts the chemical potential and determines the equilibrium transition points based on discontinuities in the fluid density.^{26,27} However, due to the discontinuous change of chemical potential, it is nontrivial to precisely determine the equilibrium transition chemical potential. Furthermore, in confined spaces, the presence of adsorption and desorption hysteresis loops makes it difficult to locate equilibrium transition points.¹⁷

In recent years, histogram-based methods²⁸⁻³² have significantly improved simulation speed and accuracy. Histogram-based methods calculate thermodynamic parameters by measuring the relative probability with which a system visits various macroscopic states.³³ One powerful algorithm is the 'flat-histogram' method, which includes three primary approaches: the multicanonical method,³⁰ Wang-Landau (WL) sampling,²⁸ and the transition-matrix (TM) method.²⁹ The WL approach also does not require prior knowledge of chemical potentials.³⁴ In the initial iterations, it efficiently samples a broad range of macrostates, thereby mitigating the risk of the system becoming trapped in preferred regions.³⁵ The WL algorithm has been extensively applied to simulate phase coexistence in CO₂³⁶ and CO₂-water mixtures,³⁷ as well as CO₂ adsorption in porous media.^{38,39} Wang-Landau transition-matrix Monte Carlo (WL-TMMC) combines three flat-histogram methods. This method can compute the distribution probabilities of macrostates (such as particle number) at given μ , V , and T . Then histogram reweighting can be used to obtain the probability distribution at various μ without requiring additional simulations.⁴⁰ Therefore, a pair of VLE points, given by vapor liquid densities and pressures at a fixed temperature, can be precisely determined in a single simulation. Furthermore, the parallel processing capability of WL-TMMC enhances its computational efficiency.^{32,41} The efficiency of WL-TMMC simulations may be further improved by using the extrapolation method to obtain thermodynamic and structural properties over a range of temperatures from a single simulation.⁴²⁻⁴⁴ Specific details of this method are listed in **Section 2.1**. This method has been used to investigate phase equilibria and surface tensions of pure/mixed n -alkanes,⁴⁵⁻⁴⁷ water,^{32,48} and even

asphaltenes⁴⁹ in bulk and/or confined spaces. However, to the best of our knowledge, there is no work utilizing parallelized WL-TMMC to study the VLE of CO₂- n -alkane binary mixtures in bulk and confined spaces.

The primary objective of this study is to assess the reliability of parallelized WL-TMMC^{32,41} in the open-source software Free Energy and Advanced Sampling Simulation Toolkit (FEASST)^{50,51} for CO₂- n -alkane VLE simulations, both in bulk and confined systems. Thus, this work serves as the first step in our ongoing research on the phase equilibria of CO₂-hydrocarbon-formation water systems within various mineral and kerogen nanopores. To achieve this, the constant volume Gibbs Ensemble (NVT-GEMC) (bulk), pore-pore GEMC (confined), and gauge-GCMC (confined) simulations are performed in the open-source software Monte Carlo for Complex Chemical Systems (MCCCS) Towhee⁵² to validate the accuracy of FEASST. Methane (C₁) and hexane (nC₆) are chosen because they are the main components of natural gas and light oil.⁵³ The results show good agreement between the phase diagrams obtained by using different methods. Additionally, the free energy distributions obtained by WL-TMMC and histogram reweighting can be used to construct the vdW loops and determine the liquid-vapor free energy barrier, which is crucial for studying adsorption hysteresis, nucleation, CO₂ miscibility processes, *etc.*

2. METHODS AND MODELS

In this section, we briefly discuss the background of each method. Detailed descriptions can be found in the following references: parallelized WL-TMMC,^{29,32,54,55} NVT-GEMC,^{14,15} pore-pore GEMC,^{16,19} and the gauge-GCMC.^{17,24}

2.1 Parallelized WL-TMMC

The fundamental principle of TMMC introduces a collection matrix C into conventional MC simulations to calculate the macrostate probability distribution. In the case of a pure component fluid, this corresponds to the grand-canonical ensemble, namely fixed chemical potential, temperature, and volume (i.e., μ, V, T). However, for mixture simulations, we fix the chemical potential of one component, the chemical potential difference between the components, the volume, and the temperature (i.e., $\mu_1, \Delta\mu_{12} = \mu_1 - \mu_2, V, T$). In both cases, the relevant macrostate variable is the total number of molecules, N_t . The matrix records every attempted transition between macrostates, regardless of whether the transition is accepted:

$$C(N_{t,o} \rightarrow N_{t,n}) = C(N_{t,o} \rightarrow N_{t,n}) + \alpha(o \rightarrow n) \quad , \quad (1)$$

$$C(N_{t,o} \rightarrow N_{t,o}) = C(N_{t,o} \rightarrow N_{t,o}) + 1 - \alpha(o \rightarrow n) \quad , \quad (2)$$

where o and n represent the old and new configurations,

respectively; $\alpha(o \rightarrow n)$ is the acceptance probability for the configuration transition from old to new,⁵⁶ which, assuming a symmetric probability to attempt a trial, can be expressed as

$$\alpha(o \rightarrow n) = \min \left[1, \frac{\pi(n)}{\pi(o)} \right], \quad (3)$$

where $\pi(n)$ and $\pi(o)$ are the probabilities of observing the new and old configurations, respectively, given by⁴²

$$\pi(n) = \frac{e^{-\beta U_p(n)}}{\Xi} \prod_{i=1}^m \frac{V^{N_i(n)} e^{\beta \mu_i N_i(n)}}{\Lambda_i^{3N_i(n)} N_i(n)!}, \quad (4)$$

where $\beta = 1/kT$, k is Boltzmann constant, U_p is the potential energy, Ξ is the grand canonical partition function, m is the number of components, N_i , μ_i , Λ_i are the molecule number, chemical potential, and de Broglie wavelength of component i , respectively.

In the TMMC simulations of this work, five trial moves are employed: translation, rotation, regrowth, insertion, and deletion. Note that $N_{t,n} = N_{t,o} \pm 1$ for insertion/deletion trials, while $N_{t,n} = N_{t,o}$ for translation, rotation, and regrowth trials. The transition probability $P(N_{t,o} \rightarrow N_{t,n})$ from $N_{t,o}$ to $N_{t,n}$ is then obtained from

$$P(N_{t,o} \rightarrow N_{t,n}) = \frac{c(N_{t,o} \rightarrow N_{t,n})}{\sum_{j=-1}^1 c(N_{t,o} \rightarrow N_{t,o+j})}. \quad (5)$$

Finally, detailed balance can be used to determine the macrostate probability

$$\Pi(N_{t,o}; \{\mu_i\}, V, T) P(N_{t,o} \rightarrow N_{t,n}) = \Pi(N_{t,n}; \{\mu_i\}, V, T) P(N_{t,n} \rightarrow N_{t,o}), \quad (6)$$

where $\Pi(N_{t,o}; \{\mu_i\}, V, T)$ is the probability of observing a total molecule number $N_{t,o}$ under fixed $\{\mu_i\}$, V , and T . Note that we use $\{\mu_i\}$ to represent μ_1 in the pure component case and μ_1 and $\Delta\mu_{12}$ in the mixture case for notational convenience.

To accurately calculate probability distributions, it is essential to collect sufficient statistics for all relevant macrostates. However, in traditional MC simulations, the probabilities of different macrostates often vary significantly. To address this issue, a bias function $\eta(N_t)$ inspired by multicanonical sampling schemes is introduced to compute the acceptance probability between configuration transitions, which can encourage the system to uniformly sample all macrostates.²⁹

$$\alpha(o \rightarrow n) = \min \left[1, \frac{\exp[\eta(N_{t,n})] \pi(n)}{\exp[\eta(N_{t,o})] \pi(o)} \right], \quad (7)$$

$$\eta(N_t) = -\ln \Pi(N_t; \{\mu_i\}, V, T). \quad (8)$$

It is important to note that while the acceptance probabilities are calculated using **Eq. (7)**, the collection matrix is still updated according to **Eq. (3)**. This ensures that previously acquired data are not discarded.²⁹

In TMMC simulations, $\Pi(N_t)$ is typically initialized with a uniform distribution, where the $\eta(N_t)$ is set as a

constant. During the initial stage, accumulating sufficient statistics in the collection matrix to estimate $\Pi(N_t)$ is time-consuming. However, once enough data have been accumulated, the system can efficiently sweep all macrostates, allowing the probability distribution to converge rapidly.⁵⁵ To accelerate TMMC simulations, the WL method²⁸ can be used to estimate an initial macrostate distribution and a bias function. Another strategy to accelerate simulation speed is parallelization.^{32, 51} Details of the WL method and parallelization strategy are presented in **Supporting Information (SI)**.

Once $\Pi(N_t)$ under the given $\{\mu_i\}$, V , and T conditions is obtained, the histogram reweighting can be used to determine the probability distribution at different chemical potentials. For pure component systems, the relationship is,²⁹

$$\ln \Pi(N_t; \mu_{1,n}, V, T) = \ln \Pi(N_t; \mu_{1,o}, V, T) + \beta N_t (\mu_{1,n} - \mu_{1,o}) + c, \quad (9)$$

where c is a normalization constant. For binary mixture systems, the relationship is,⁵⁴

$$\ln \Pi(N_t; \{\mu_{1,n}, \Delta\mu_{12}\}, V, T) = \ln \Pi(N_t; \{\mu_{1,o}, \Delta\mu_{12}\}, V, T) + \beta N_t (\mu_{1,n} - \mu_{1,o}) + c. \quad (10)$$

In other words, the chemical potential difference between the two components remains unchanged before and after histogram reweighting. Using **Eq. (9)** or **(10)**, the chemical potential at VLE can be determined, where the areas under the two local maxima of the probability distribution curve are equal. The N_t separating the vapor and liquid phases corresponds to the local minimum between the two local maxima.^{29, 57}

With the $\Pi(N_t)$ at VLE, the average molecule number in each phase can be obtained

$$\langle N_i^{g \text{ or } l} \rangle = \frac{\sum_{N_t \in g \text{ or } l} \bar{N}_i \Pi(N_t)}{\sum_{N_t \in g \text{ or } l} \Pi(N_t)}, \quad (11)$$

where g and l represent the vapor and liquid phases, respectively. \bar{N}_i is the average molecule number of component i at a specific N_t , which can be recorded by adding a bookkeeping code to the WL-TMMC simulations. The mole fraction and density of each phase can then be calculated by

$$x_i \text{ or } y_i = \frac{\langle N_i^{g \text{ or } l} \rangle}{\sum_i \langle N_i^{g \text{ or } l} \rangle}, \quad (12)$$

$$\rho_g \text{ or } \rho_l = \frac{\sum_i M_i \langle N_i^{g \text{ or } l} \rangle}{N_A V}, \quad (13)$$

where x_i and y_i are the mole fractions of component i in the vapor and liquid phases, respectively; ρ is the mass density, M is the molar mass, and N_A is Avogadro's constant. For simulations in the bulk phase, the VLE pressure P can also be obtained,⁵⁸

$$\beta P g \text{ or } l V = \ln \left[\sum_{N_t \in g \text{ or } l} \Pi(N_t; \{\mu_i^{\text{VLE}}\}, V, T) \right] - \ln \Pi(0; \{\mu_i^{\text{VLE}}\}, V, T). \quad (14)$$

2.2 NVT-GEMC, pore-pore GEMC and Gauge-GCMC

NVT-GEMC and pore-pore GEMC both employ two boxes to simulate phase equilibria.^{14, 16} The NVT-GEMC uses two bulk boxes (**Figure 1 (a)**), while pore-pore GEMC uses two confined boxes (**Figure 1 (b)**). Five types of trial moves are mainly employed: translation, rotation and regrowth within each box, as well as volume exchange and particle swap between boxes. During the simulations, the total number of molecules and the total volume of the two boxes are fixed. We note that pore-pore GEMC is designed to simulate the VLE of confined fluids. During volume exchange, the walls of both boxes are scaled accordingly. Thus, it is difficult to apply it to irregular pores. However, in this work, the pore walls are characterized as ideal surfaces using the 10-4-3 Steele potential (see **Section 2.3**), which can be safely scaled.¹⁹ In this work, to maintain a constant pore size, pore-pore GEMC scales the box only in the x - and y -directions, while NVT-GEMC performs isotropic scaling in all three directions.

The gauge-GCMC also uses two simulation boxes.^{17, 24} One box, the confined one, is used to simulate the confined fluid, while the other, the gauge one (see **Figure 1 (a)**), is used to constrain density fluctuations of the confined fluid. For binary mixture simulations, the chemical potential of component 1 is fixed in the gauge box, while the total number of component 2 molecules across both boxes remains constant. Five types of trial moves are employed: translation, rotation, regrowth within each box, insertion and deletion moves for component 1 in the gauge box, and particle swaps between the two boxes.

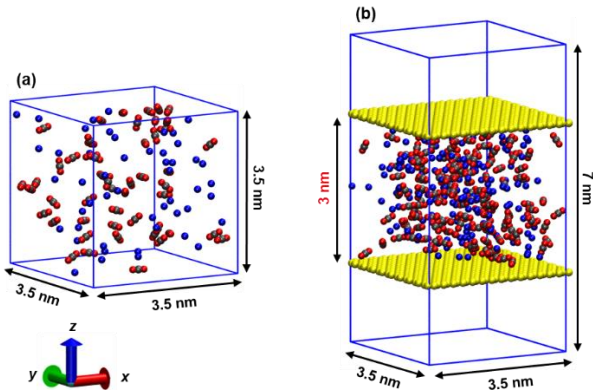


Figure 1. MC simulation boxes: (a) bulk box and (b) confined box. Red, gray, and blue balls are the CO₂ oxygen, the CO₂ carbon, and the methane atoms, respectively. The yellow walls represent the virtual surfaces of 10-4-3 Steele potential.⁵⁹ The figure was generated by open source software VMD.⁶⁰

2.3 Simulation Details

The TraPPE-UA force field⁶¹ and the TraPPE-EH⁶² force field are used to model n -alkanes and CO₂ molecules,

respectively. Nonbonded interactions between fluid atoms are calculated using 12-6 Lennard-Jones (L-J) potentials,

$$U_{\text{nb}}(r_{ij}) = 4\varepsilon_{ij} \left[\left(\frac{\sigma_{ij}}{r_{ij}} \right)^{12} - \left(\frac{\sigma_{ij}}{r_{ij}} \right)^6 \right], \quad (15)$$

where r_{ij} is the distance between atom i and j , ε_{ij} is the potential well depth, and σ_{ij} is the L-J size. The Lorentz-Berthelot (L-B) combining rules⁶³ are used to compute ε_{ij} and σ_{ij} between different atom types. The 1-4 intramolecular L-J and Coulomb (see below) interactions are excluded, meaning that nonbonded interactions between atoms separated by three or fewer consecutive bonds in the molecular topology are not considered. The cutoff distance is set to 1.4 nm, and tail corrections⁶⁴ are applied to L-J interactions beyond the cutoff. Theoretically, in rigorously confined space simulations, tail corrections should either be disabled or further modified along the confined z -direction.^{19, 65} However, the purpose of this study is to validate the reliability of the WL-TMMC in FEASST. Therefore, ensuring consistency in simulation settings between FEASST and MCCCSTowhee is sufficient. The non-bonded interactions between fluid and solid walls are described by 10-4-3 Steele potentials,⁵⁹

$$\varphi_{\text{wf}}(z) = 2\pi\rho_{\text{w}}\varepsilon_{\text{wf}}\sigma_{\text{wf}}^2\Delta \left[\frac{2}{5} \left(\frac{\sigma_{\text{wf}}}{z} \right)^{10} - \left(\frac{\sigma_{\text{wf}}}{z} \right)^4 - \frac{\sigma_{\text{wf}}^4}{3\Delta(0.61\Delta+z)^3} \right], \quad (16)$$

where ρ_{w} is the density of solid atoms, Δ is the spacing between the solid layers, and ε_{wf} and σ_{wf} are the potential parameters between walls and fluid atoms, also calculated by L-B mixing rules. In addition, the fluid-wall interactions shift to zero at a cutoff distance of 1.4 nm. However, in MCCCSTowhee, each Steele wall can only have one surface interacting with fluid atoms, and non-periodic boundaries cannot be set. In contrast, in FEASST, both surfaces of the Steele wall interact with fluid atoms. To ensure consistency in the impact of Steele walls between the two software, 2 nm vacuum spaces are added above and below the pores, as shown in **Figure 1 (b)**. For CO₂ molecules, the bonds and angles are treated as rigid. Therefore, all bonded interactions are excluded. For $n\text{C}_6$ molecules, the bond lengths are fixed, while the bond and dihedral angles are allowed to vibrate. The bond bending energy and torsional energy are expressed as

$$U_{\text{bend}}(\theta) = \frac{1}{2}k_{\theta}(\theta - \theta_{\text{eq}})^2, \quad (17)$$

$$U_{\text{torsion}}(\phi) = c_1(1 + \cos\phi) + c_2(1 - \cos 2\phi) + c_3(1 + \cos 3\phi), \quad (18)$$

where θ_{eq} is the equilibrium bond angle, ϕ is the dihedral angle, and k_{θ} , c_0 , c_1 , c_2 , and c_3 are the force constants. Long-range electrostatics are described by the Coulomb potential,

$$U_{\text{coul}} = \frac{q_i q_j}{4\pi\varepsilon_0 r_{ij}}, \quad (19)$$

where q_i is the partial charge, ϵ_0 is the dielectric constant, set to 1.0. The Ewald summation is used to calculate the Coulomb potential, with screening parameter $\alpha = 5.6/3.5 \text{ nm}^{-1}$ and maximum wave vector $k_{\text{max}} = 6$ in all three directions. Again, the periodic interaction contribution along the z -direction should be removed. FEASST allows for applying slab corrections;⁶⁶ however, MCCCSTowhee can only address this issue by adding a sufficiently large vacuum space, typically 3–5 times of the pore size.¹¹ Adding such a large space will significantly slow the simulation. Therefore, since our primary objective is to compare the consistency of results obtained from different methods, no extra vacuum layers are added (still 2 nm). All the force field parameters are listed in **Table S1** and **Table S2** of **SI**.

As shown in **Figure 1**, the simulation box for the bulk fluid has initial dimensions of $3.5 \times 3.5 \times 3.5 \text{ nm}^3$ in the x -, y -, and z -directions, while the box for the confined fluid initially measures $3.5 \times 3.5 \times 7 \text{ nm}^3$. In the confined box, the pore has a dimension of 3 nm along the z -direction, with the remaining space being vacuum. A hard potential is applied to the vacuum to prevent molecules from entering. The temperature for the $\text{CO}_2\text{-C}_1$ and $\text{CO}_2\text{-nC}_6$ systems is set to 250 K and 313.15 K, respectively. For the bulk fluid VLE pressure, the NVT-GEMC simulations provide a direct output, while the WL-TMMC simulations calculate it using **Eq. (14)**. For the confined fluid, an additional bulk GCMC simulation with the same chemical potential as the confined fluid is performed, and the bulk pressure is used to represent the VLE pressure.

To ensure the convergence of $\Pi(N_t)$, FEASST simulations were run for 10 sweeps, where a sweep is defined as each N_t being visited from a different one at least 100 times.⁶⁷ To improve the sampling and convergence of these simulations, the dual-cut configurational bias (DCCB)^{68, 69} MC method was employed for the regrowth and insertion/deletion moves of hexane. At VLE, the maximum total number of molecules $N_{t,\text{max}}$ in the simulation was determined by²⁹

$$\ln\Pi(N_t^1)_{\text{max}} - \ln\Pi(N_{t,\text{max}}) > 10, \quad (20)$$

where $\ln\Pi(N_t^1)_{\text{max}}$ is the maximum probability in the liquid phase. Each simulation in MCCCSTowhee consists of 50 million trials, with 20 million trials used for system equilibration and 30 million trials for sampling. The configurational bias (CB) MC method described by Martin and Frischknecht⁷⁰ was used for regrowth, particle exchange between boxes, and insertion/deletion moves of

hexane. The probability of different trial moves is listed in **Table S3** in **SI**. For NVT-GEMC and pore-pore GEMC simulations, we used the composition and density data obtained from the WL-TMMC simulations as the basis for determining the initial configuration. In the $\text{CO}_2\text{-C}_1$ gauge-GCMC simulations, we fixed the chemical potential of C_1 , whereas in the $\text{CO}_2\text{-nC}_6$ simulations, we fixed the chemical potential of CO_2 .

3. RESULTS AND DISCUSSION

3.1 Phase Diagrams

The lower part of **Figure 2 (a)** shows the $\ln\Pi(N_t)$ distribution for the $\text{CO}_2\text{-C}_1$ system when $\beta\Delta\mu_{12} = 0.8$. An example input file for the confined $\text{CO}_2\text{-nC}_6$ system, along with the corresponding output probability distribution file, is provided in the **SI**. The dashed lines represent the simulation results of WL-TMMC, while the solid lines represent $\ln\Pi(N_t)$ at VLE, calculated by histogram reweighting, **Eq. (10)**. The dotted line indicates the $\ln\Pi(N_t)$ of the bulk phase reweighted to $\{\mu_i\} = \{\mu_i^{\text{VLE}}\}_{\text{confined}}$. By combining the average number of C_1 molecules at each N_t as shown in the upper part of **Figure 2 (a)**, the x/y - P and ρ - P diagrams for VLE can be constructed. **Figure 2 (b)** shows the dependence of the confined fluid density and the molar fraction of C_1 on the chemical potential of CO_2 . The density clearly exhibits a vdW loop. In this work, the loop is initially fitted with a polynomial, and the Maxwell equal-area rule is then applied to determine the VLE density and chemical potential,²⁴

$$\int_A^B \rho d\mu_{\text{CO}_2} + \int_B^C \rho d\mu_{\text{CO}_2} + \int_C^D \rho d\mu_{\text{CO}_2} = 0. \quad (21)$$

The determination of the VLE molar fraction follows a similar procedure: first, the simulation data are fitted with a polynomial, and then the VLE molar fraction is determined using the VLE chemical potential. The NVT-GEMC and pore-pore GEMC are relatively simpler for constructing phase diagrams, as the composition and density data can be directly outputted. **Figure 2 (c)** gives an example of the $\text{CO}_2\text{-nC}_6$ case in the pore-pore GEMC system. At the beginning, within the same box, the system fluctuates between the liquid and vapor phase. This implies that, under these conditions, the density fluctuations in the mixture readily overcome the liquid-vapor free energy barrier (will be discussed in **Section 3.2**).

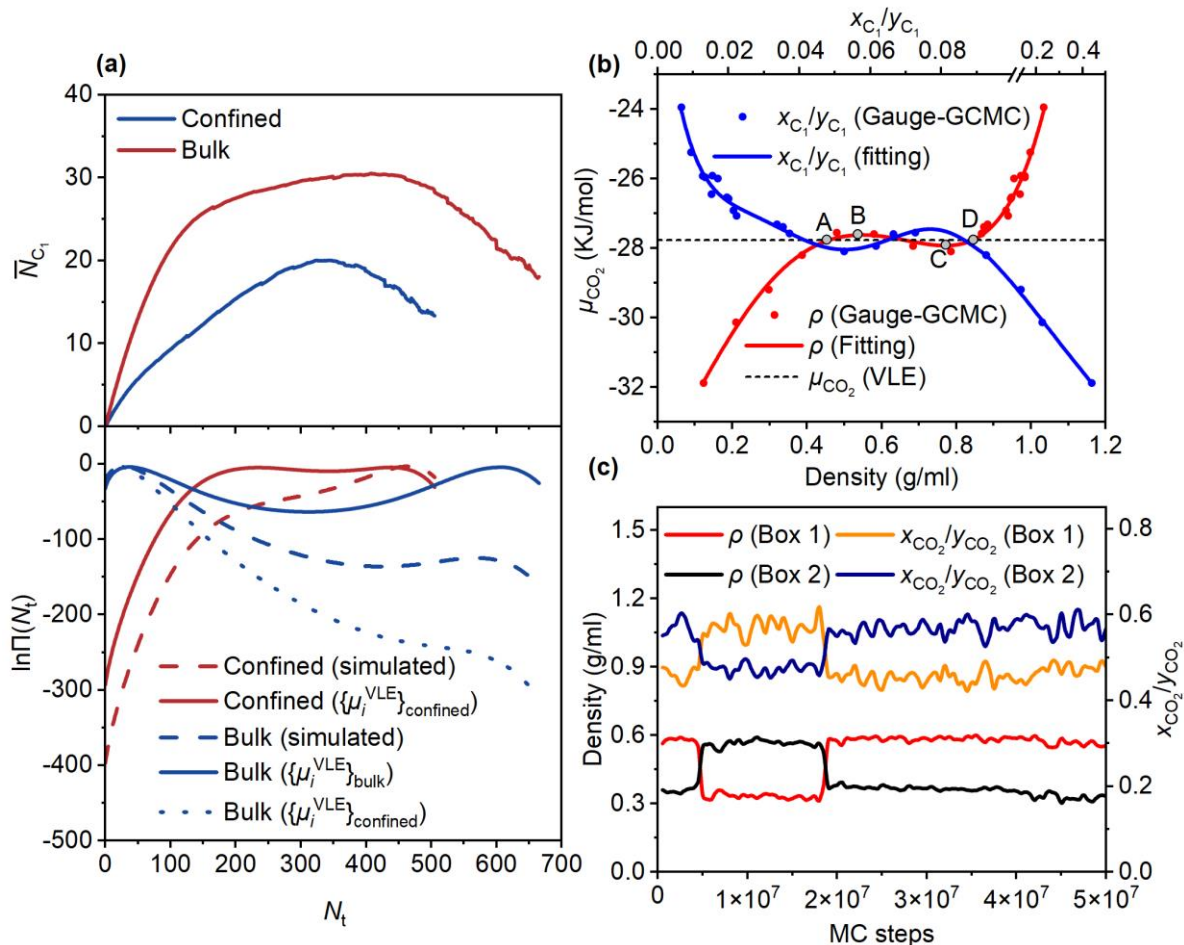


Figure 2. (a) Upper: average number of C_1 at each N_t ; lower: N_t probability distribution of the CO_2 - C_1 system with $\beta\Delta\mu_{12} = 0.8$. The dashed lines are generated by WL-TMMC, while the solid and dotted lines are obtained by histogram reweighting. (b) CO_2 - C_1 van der Waals loop generated by gauge-GCMC simulations with chemical potential of C_1 fixed at 27.44 kJ/mol (3300 K), A and D are binodal points, while B and C are spinodal points. (c) Density and composition fluctuation of CO_2 - nC_6 in pore-pore GEMC simulation boxes.

The simulated x/y - P and ρ - P phase diagrams are presented in **Figure 3**. The x/y - ρ diagrams are provided in **Figure S1**. The values and standard errors are also provided in Tables S4 and S5, but the standard errors are omitted here for the sake of clarity. For the bulk phase systems, the results obtained using WL-TMMC exhibit excellent agreement with those from NVT-GEMC and published simulation data.^{5, 71} For the confined systems, no literature data are available. However, apart from slight differences at specific points in the ρ - P diagrams, the results of WL-TMMC are generally in good agreement with those obtained from the Gauge-GCMC and Pore-Pore GEMC simulations. This discrepancy may be attributed to manual fitting in the Gauge-GCMC method, density fluctuations in Pore-Pore GEMC simulations (as shown in **Figure 2**), as well as the inherent drawbacks of Pore-Pore GEMC due to the necessity of scaling the wall surface.¹⁷ **Table 1** shows the relative errors of each result compared to the WL-TMMC calculation results, with the calculation methods provided in **Figure S2** and **Eq. (S6) - (S8)**. The relative errors of bulk-phase results are less than

6%, while those of confined results are less than 8%. Thus, the WL-TMMC implemented in FEASST is generally reliable. Compared to the bulk phase, the confined x/y - P diagrams are significantly compressed. Although $\Delta\mu_{12}$ is the same, the corresponding bulk-phase pressure at the VLE is much lower. As shown by the dotted line in **Figure 2 (a)**, when the confined systems reach VLE, the corresponding bulk-phase systems remain in states with only stable vapor phase (see **Section 3.2**). This occurs because confined spaces reduce the molar fractions of light components in the vapor phase while increasing their fractions in the liquid phase. Consequently, the vapor-phase density increases, while the liquid-phase density decreases in the ρ - P phase diagrams, thereby reducing the differences between the two phases and promoting the realization of VLE. Furthermore, the confinement effect is more pronounced on the vapor phase properties, as evident by the shift in density and molar fraction of light components shown in **Figure 3**.

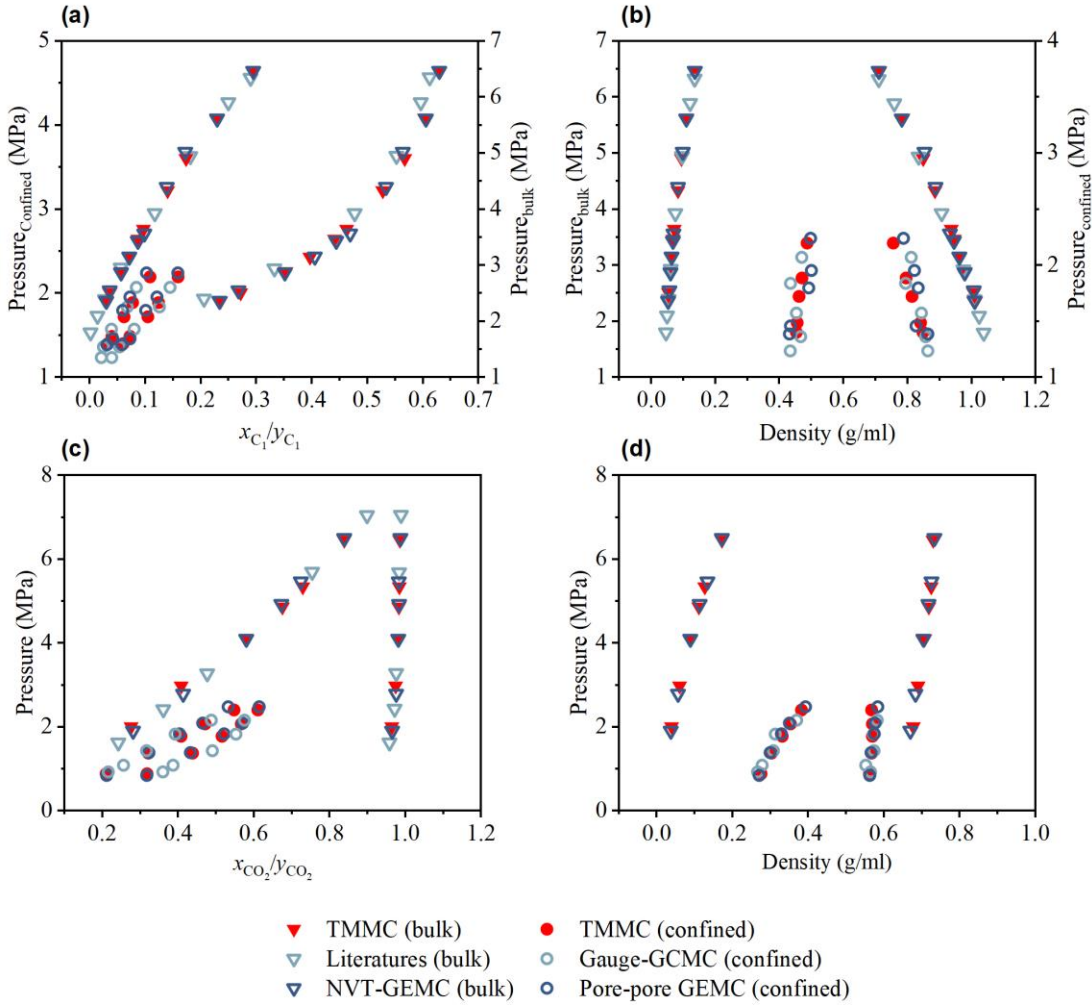


Figure 3. Phase diagrams in bulk and confined spaces. (a) x/y - P diagrams of CO_2 - C_1 ; (b) ρ - P diagrams of CO_2 - C_1 ; (c) x/y - P diagrams of CO_2 - nC_6 ; (d) ρ - P diagrams of CO_2 - nC_6 . The literature data for CO_2 - C_1 systems is from Zimmermann *et al.*,⁷¹ while the data for CO_2 - nC_6 systems is from Vishnyakov *et al.*⁵ Adapted with permission from ref. 71. Copyright 2024 Springer Nature. Adapted with permission from ref. 5. Copyright 2020 Elsevier.

Table 1. Relative Errors Compared to WL-TMMC, Details are Provided in Supporting Information

System	Phase diagram	Literature data	NVT-GEMC	gauge-GCMC	Pore-pore GEMC
CO_2 - C_1	x/y - P	4.19%	2.54%	7.64%	7.82%
	ρ - P	1.36%	0.82%	2.67%	3.81%
	x/y - ρ	3.17%	2.53%	2.28%	3.49%
CO_2 - nC_6	x/y - P	2.80%	1.86%	4.27%	2.43%
	ρ - P	/	0.88%	2.23%	1.26%
	x/y - ρ	/	5.86%	3.24%	2.54%

3.2 Free Energy and van der Waals Loops

Free energy may be obtained from the macrostate distribution, $\ln\Pi(N_t)$, by relating the grand potential,

$$\Omega = -kT \ln \Xi(\mu_1, \mu_2, V, T),^{72} \text{ to Eq. 4 of Ref. 42,}$$

$$\ln\Pi(N_t) = \beta\mu_1 N_t + \ln Y(N_t, \Delta\mu_{12}, V, T) - \ln \Xi(\mu_1, \mu_2, V, T), \quad (22)$$

where Υ is the isochoric semigrand ensemble partition function, Ξ is the grand canonical partition function, and coexistence can be found by equating the probability of the two phases. When $\ln\Pi(N_t)$ exhibits a single local maximum, the system has only one stable phase. If there are two local maxima, the larger corresponds to the stable phase, while the smaller corresponds to the metastable phase.^{42, 54, 56, 58} The local minimum between the two phases corresponds to the unstable phase. Thus, by combining these criteria and the histogram reweighting, the WL-TMMC enables the construction of a complete vdW loop. As illustrated in **Figure 4 (a)**, the VLE points identified from the vdW loop using **Eq. (21)** are completely consistent with the results obtained by the equal probability criterion. This approach not only enables the loop construction from a single simulation, but also allows the determination of thousands of points,

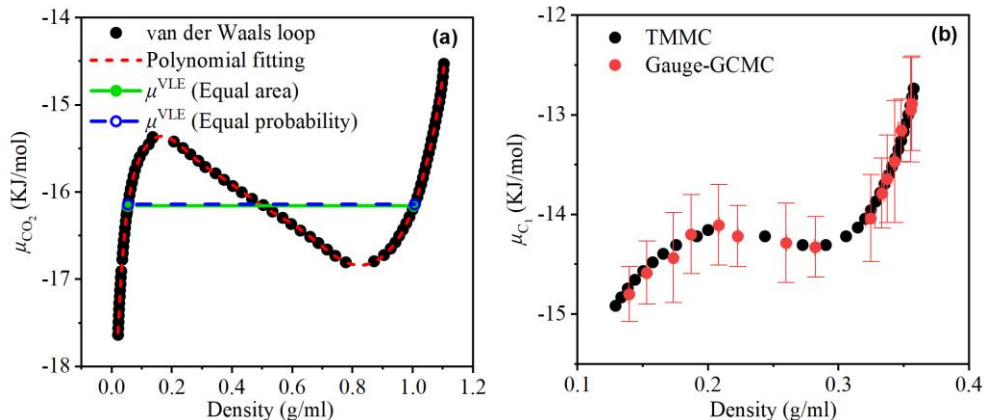


Figure 4 (a) van der Waals loop generated by WL-TMMC of the CO₂-C₁ system with $\beta\Delta\mu_{12} = 0.8$. (b) Comparison of van der Waals loops generated by WL-TMMC and gauge-GCMC of C₁ systems with $T = 150\text{K}$. When the density is low, the error bars are smaller than the symbol size. The results of TMMC shifted downward by approximately 3.72 kJ/mol due to the difference in the normalization constants when calculating chemical potentials.

When the system exhibits VLE, the liquid-vapor free energy barrier can be estimated by,⁷⁴

$$\beta\Delta F \approx \frac{1}{2} \left[\ln\Pi(N_t^l)_{\max} + \ln\Pi(N_t^g)_{\max} \right] - \ln\Pi(N_t)_{\text{local min.}} \quad (23)$$

where the approximation comes from using the $\ln\Pi(N_t)$ instead of the fully two-dimensional $\ln\Pi(N_1, N_2)$ and obtaining the saddle point.⁷⁵ This barrier may exhibit significant dependence on system size; therefore, finite-size scaling is necessary to obtain the interfacial tension.⁷⁴⁻⁷⁶ The energy barriers in the bulk and confined systems are shown in **Figure 5**. As pressure increases, the energy barrier decreases, indicating that the fluid is approaching the critical state. In addition, at the same pressure, the energy barrier in the confined space is reduced, implying that the critical pressure is also lower. The P - F curves can be appropriately fitted and extrapolated to the points where $\Delta F = 0$, which corresponds to the critical pressure at the given temperature. In fact, the energy barrier is related to the vapor-liquid interfacial tension,^{74, 77, 78} making this

showcasing the remarkable efficiency of the WL-TMMC. In a binary system, this method constructs the vdW loop by varying μ_1 and μ_2 while fixing $\Delta\mu_{12}$. In contrast, gauge-GCMC constructs the loop by fixing μ_1 and adjusting μ_2 . Consequently, these two methods can complement each other, and the vdW loop can play an important role in studying adsorption hysteresis in nanopores⁵⁶ and identifying transient states in nucleation processes.^{20, 73} Due to the different construction mechanisms, comparing the vdW loops generated by both methods in a binary system requires additional multiset simulations, which is outside the scope of this work. Therefore, we focus here on comparing the loops formed by pure component methane systems in confined spaces. For the gauge-GCMC, this only requires fixing the number of methane molecules. As shown in **Figure 4 (b)**, the two vdW loops are in good agreement.

method similar to the vanishing interfacial tension approach for determining the critical points.⁷⁹

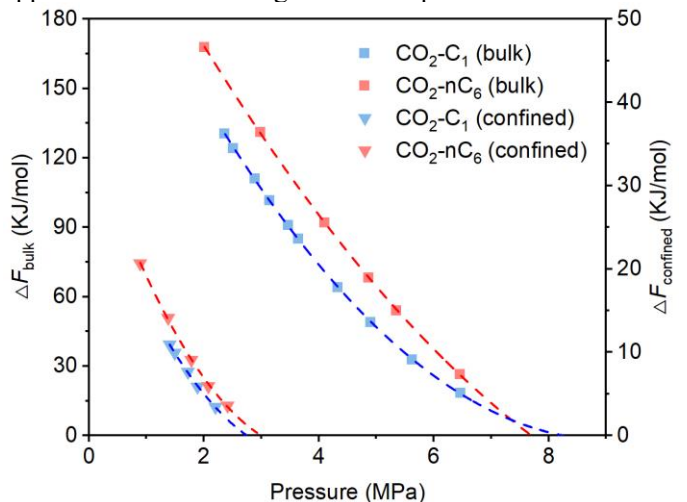


Figure 5. Liquid-vapor free energy barrier in bulk and confined spaces.

4. SUMMARY AND CONCLUSIONS

In this study, WL-TMMC implemented in the FEASST is used to simulate the VLE of CO₂-C₁ and CO₂-nC₆ in both bulk and confined spaces. Validation is conducted using NVT-GEMC (bulk), pore-pore GEMC (confined), and gauge-GCMC (confined) simulations in the MCCCSTowhee software. The FEASST simulation results exhibit strong consistency with literature data and results from MCCCSTowhee. For confined systems, the WL-TMMC, when combined with histogram reweighting, requires only a single simulation to accurately determine a pair of VLE points, and is not constrained by pore geometry. This method provides free energy information that can distinguish between stable, metastable, and unstable fluid states, allowing for the construction of a complete vdW loop from a single simulation. In addition, the resulting liquid-vapor free energy barrier offers a method for determining the critical points, consistent with the vanishing interfacial tension approach.

In conclusion, the WL-TMMC in FEASST is a reliable tool for studying the CO₂-*n*-alkane VLE and can be applied to future studies. For example, studying the minimum miscible pressure (MMP) and adsorption behaviors of CO₂ and *n*-alkanes in the nanopores of shale minerals and kerogen. In addition, this method may be extended to systems with ternary or more components.⁵⁴ Therefore, studying the three-phase equilibrium of CO₂-hydrocarbon-water systems in the presence of connate water is also feasible.

5. SUPPORTING INFORMATION

Wang-Landau method and parallel strategy of FEASST; Nonbonded and bonded potential parameters; Probability of different MC trial moves; VLE data and stand errors; *x/y-ρ* diagrams; Calculation process of relative errors; Example input file for the confined CO₂-nC₆ system

(1) Dai, Z.; Middleton, R.; Viswanathan, H.; Fessenden-Rahn, J.; Bauman, J.; Pawar, R.; Lee, S.-Y.; McPherson, B. An integrated framework for optimizing CO₂ sequestration and enhanced oil recovery. *Environmental Science & Technology Letters* **2014**, *1* (1), 49-54.

(2) Song, Z.; Li, Y.; Song, Y.; Bai, B.; Hou, J.; Song, K.; Jiang, A.; Su, S. A critical review of CO₂ enhanced oil recovery in tight oil reservoirs of North America and China. In *SPE Asia Pacific Oil and Gas Conference and Exhibition*, 2020; SPE: p D011S005R002.

(3) Shi, Y.; Yang, Z.; Peng, J.; Zhou, M.; Song, X.; Cui, Q.; Fan, M. CO₂ storage characteristics and migration patterns under different abandoned oil and gas well types. *Energy* **2024**, *292*, 130545.

(4) Kopp, A.; Binning, P. J.; Johannsen, K.; Helmig, R.; Class, H. A contribution to risk analysis for leakage

through abandoned wells in geological CO₂ storage. *Advances in Water Resources* **2010**, *33* (8), 867-879.

(5) Vishnyakov, A.; Weathers, T.; Hosangadi, A.; Chiew, Y. C. Molecular models for phase equilibria of alkanes with air components and combustion products I. Alkane mixtures with nitrogen, CO₂ and water. *Fluid Phase Equilibria* **2020**, *514*, 112553.

(6) Wang, W.; Wen, J.; Wang, C.; Gomari, S. R.; Xu, X.; Zheng, S.; Su, Y.; Li, L.; Hao, Y.; Li, D. Current status and development trends of CO₂ storage with enhanced natural gas recovery (CS-EGR). *Fuel* **2023**, *349*, 128555.

(7) Telmadarreie, A.; Doda, A.; Trivedi, J. J.; Kuru, E.; Choi, P. CO₂ microbubbles—A potential fluid for enhanced oil recovery: Bulk and porous media studies. *Journal of Petroleum Science and Engineering* **2016**, *138*, 160-173.

(8) Li, X.; Peng, B.; Liu, Q.; Liu, J.; Shang, L. Micro and nanobubbles technologies as a new horizon for CO₂-EOR and CO₂ geological storage techniques: A review. *Fuel* **2023**, *341*, 127661.

(9) Dindoruk, B.; Johns, R.; Orr Jr, F. M. Measurement and modeling of minimum miscibility pressure: A state-of-the-art review. *SPE Reservoir Evaluation & Engineering* **2021**, *24* (02), 367-389.

(10) Ross, D. J.; Bustin, R. M. The importance of shale composition and pore structure upon gas storage potential of shale gas reservoirs. *Marine and petroleum Geology* **2009**, *26* (6), 916-927.

(11) Zhang, M.; Zhan, S.; Jin, Z. Recovery mechanisms of hydrocarbon mixtures in organic and inorganic nanopores during pressure drawdown and CO₂ injection from molecular perspectives. *Chemical Engineering Journal* **2020**, *382*, 122808.

(12) Han, Y.; Mahlstedt, N.; Horsfield, B. The Barnett Shale: Compositional fractionation associated with intraformational petroleum migration, retention, and expulsion. *AAPG Bulletin* **2015**, *99* (12), 2173-2202.

(13) Tissot, B. P.; Welte, D. H. *Petroleum formation and occurrence*; Springer Science & Business Media, 2013.

(14) Panagiotopoulos, A. Z. Direct determination of phase coexistence properties of fluids by Monte Carlo simulation in a new ensemble. *Molecular Physics* **1987**, *61* (4), 813-826.

(15) Panagiotopoulos, A. Z.; Quirke, N.; Stapleton, M.; Tildesley, D. Phase equilibria by simulation in the Gibbs ensemble: alternative derivation, generalization and application to mixture and membrane equilibria. *Molecular Physics* **1988**, *63* (4), 527-545.

(16) Panagiotopoulos, A. Z. Adsorption and capillary condensation of fluids in cylindrical pores by Monte Carlo simulation in the Gibbs ensemble. *Molecular Physics* **1987**, *62* (3), 701-719.

(17) Neimark, A. V.; Vishnyakov, A. Gauge cell method for simulation studies of phase transitions in confined systems. *Physical Review E* **2000**, *62* (4), 4611.

(18) Liu, L.; Nieto-Draghi, C.; Lachet, V.; Heidaryan,

- E.; Aryana, S. A. Bridging confined phase behavior of CH₄-CO₂ binary systems across scales. *The Journal of Supercritical Fluids* **2022**, *189*, 105713.
- (19) Sobacki, N.; Nieto-Draghi, C.; Di Lella, A.; Ding, D. Y. Phase behavior of hydrocarbons in nano-pores. *Fluid Phase Equilibria* **2019**, *497*, 104-121.
- (20) Vishnyakov, A.; Neimark, A. V. Multicomponent gauge cell method. *The Journal of chemical physics* **2009**, *130* (22), 224103.
- (21) Li, J.; Rao, Q.; Xia, Y.; Hoepfner, M.; Deo, M. D. Confinement-mediated phase behavior of hydrocarbon fluids: Insights from Monte Carlo simulations. *Langmuir* **2020**, *36* (26), 7277-7288.
- (22) Jiang, J.; Sandler, S. I.; Smit, B. Capillary phase transitions of n-alkanes in a carbon nanotube. *Nano Letters* **2004**, *4* (2), 241-244.
- (23) Vishnyakov, A.; Piotrovskaya, E.; Brodskaya, E.; Votyakov, E.; Tovbin, Y. K. Critical properties of Lennard-Jones fluids in narrow slit-shaped pores. *Langmuir* **2001**, *17* (14), 4451-4458.
- (24) Jin, B.; Nasrabadi, H. Phase behavior of multi-component hydrocarbon systems in nano-pores using gauge-GCMC molecular simulation. *Fluid Phase Equilibria* **2016**, *425*, 324-334.
- (25) Xing, X.; Feng, Q.; Zhang, W.; Wang, S. Vapor-liquid equilibrium and criticality of CO₂ and n-heptane in shale organic pores by the Monte Carlo simulation. *Fuel* **2021**, *299*, 120909.
- (26) Cao, J.; Liang, Y.; Masuda, Y.; Tamura, K.; Ishiwata, T.; Ohtsuki, S.; Ito, Y.; Matsuoka, T. Phase behavior of methane/n-butane binary mixtures in organic nanopores under bulk vapor conditions. *Energy & Fuels* **2022**, *36* (24), 14748-14759.
- (27) Dantas, S.; Struckhoff, K. C.; Thommes, M.; Neimark, A. V. Phase behavior and capillary condensation hysteresis of carbon dioxide in mesopores. *Langmuir* **2019**, *35* (35), 11291-11298.
- (28) Wang, F.; Landau, D. P. Efficient, multiple-range random walk algorithm to calculate the density of states. *Physical review letters* **2001**, *86* (10), 2050.
- (29) Errington, J. R. Direct calculation of liquid-vapor phase equilibria from transition matrix Monte Carlo simulation. *The Journal of chemical physics* **2003**, *118* (22), 9915-9925.
- (30) Berg, B. A.; Neuhaus, T. Multicanonical ensemble: A new approach to simulate first-order phase transitions. *Physical Review Letters* **1992**, *68* (1), 9.
- (31) Guo, W.; Bali, P.; Errington, J. R. Calculation of the Saturation Properties of a Model Octane-Water System Using Monte Carlo Simulation. *The Journal of Physical Chemistry B* **2018**, *122* (23), 6260-6271.
- (32) Rane, K. S.; Murali, S.; Errington, J. R. Monte Carlo simulation methods for computing liquid-vapor saturation properties of model systems. *Journal of chemical theory and computation* **2013**, *9* (6), 2552-2566.
- (33) Chipot, C. In *Free Energy Calculations*. Springer: 2007.
- (34) Ganzenmüller, G.; Camp, P. J. Applications of Wang-Landau sampling to determine phase equilibria in complex fluids. *The Journal of Chemical Physics* **2007**, *127* (15), 154504.
- (35) Escobedo, F. A.; Abreu, C. R. On the use of transition matrix methods with extended ensembles. *The Journal of chemical physics* **2006**, *124* (10), 104110.
- (36) Desgranges, C.; Delhommelle, J. Evaluation of the grand-canonical partition function using expanded Wang-Landau simulations. I. Thermodynamic properties in the bulk and at the liquid-vapor phase boundary. *The Journal of Chemical Physics* **2012**, *136* (18), 184107.
- (37) Desgranges, C.; Delhommelle, J. Evaluation of the grand-canonical partition function using expanded Wang-Landau simulations. III. Impact of combining rules on mixtures properties. *The Journal of Chemical Physics* **2014**, *140* (10), 104109.
- (38) Hicks, J. M.; Desgranges, C.; Delhommelle, J. Characterization and Comparison of the Performance of IRMOF-1, IRMOF-8, and IRMOF-10 for CO₂ Adsorption in the Subcritical and Supercritical Regimes. *The Journal of Physical Chemistry C* **2012**, *116* (43), 22938-22946.
- (39) Desgranges, C.; Delhommelle, J. Evaluation of the grand-canonical partition function using expanded Wang-Landau simulations. II. Adsorption of atomic and molecular fluids in a porous material. *The Journal of Chemical Physics* **2012**, *136* (18), 184108.
- (40) Ferrenberg, A. M.; Swendsen, R. H. New Monte Carlo technique for studying phase transitions. *Physical review letters* **1988**, *61* (23), 2635.
- (41) Hatch, H. W.; Siderius, D. W.; Errington, J. R.; Shen, V. K. Efficiency Comparison of Single-and Multiple-Macrostate Grand Canonical Ensemble Transition-Matrix Monte Carlo Simulations. *The Journal of Physical Chemistry B* **2023**, *127* (13), 3041-3051.
- (42) Mahynski, N. A.; Errington, J. R.; Shen, V. K. Temperature extrapolation of multicomponent grand canonical free energy landscapes. *The Journal of Chemical Physics* **2017**, *147* (5), 054105.
- (43) Mahynski, N. A.; Hatch, H. W.; Witman, M.; Sheen, D. A.; Errington, J. R.; Shen, V. K. Flat-histogram extrapolation as a useful tool in the age of big data. *Molecular Simulation* **2021**, *47* (5), 395-407.
- (44) Monroe, J. I.; Hatch, H. W.; Mahynski, N. A.; Shell, M. S.; Shen, V. K. Extrapolation and interpolation strategies for efficiently estimating structural observables as a function of temperature and density. *The Journal of chemical physics* **2020**, *153* (14), 144101.
- (45) Singh, J. K.; Errington, J. R. Calculation of phase coexistence properties and surface tensions of n-alkanes with grand-canonical transition-matrix Monte Carlo simulation and finite-size scaling. *The Journal of Physical Chemistry B* **2006**, *110* (3), 1369-1376.
- (46) Singh, S. K.; Sinha, A.; Deo, G.; Singh, J. K.

Vapor– liquid phase coexistence, critical properties, and surface tension of confined alkanes. *The Journal of Physical Chemistry C* **2009**, *113* (17), 7170-7180.

(47) Chakraborti, T.; Adhikari, J. Phase equilibria and critical point predictions of mixtures of molecular fluids using grand canonical transition matrix Monte Carlo. *Industrial & Engineering Chemistry Research* **2017**, *56* (22), 6520-6534.

(48) Datar, A.; Witman, M.; Lin, L. C. Monte Carlo simulations for water adsorption in porous materials: Best practices and new insights. *AIChE Journal* **2021**, *67* (12), e17447.

(49) Rane, K. S.; Kumar, V.; Wierchowski, S.; Shaik, M.; Errington, J. R. Liquid–vapor phase behavior of asphaltene-like molecules. *Industrial & Engineering Chemistry Research* **2014**, *53* (45), 17833-17842.

(50) Hatch, H. W.; Mahynski, N. A.; Shen, V. K. FEASST: Free energy and advanced sampling simulation toolkit. *Journal of Research of the National Institute of Standards and Technology* **2018**, *123*, 1.

(51) Hatch, H. W.; Siderius, D. W.; Shen, V. K. Monte Carlo molecular simulations with FEASST version 0.25. 1. *The Journal of Chemical Physics* **2024**, *161* (9), 092501.

(52) Martin, M. G. MCCCSTowhee: a tool for Monte Carlo molecular simulation. *Molecular Simulation* **2013**, *39* (14-15), 1212-1222.

(53) Wang, W.; Xu, J.; Zhan, S.; Xie, Q.; Wang, C.; Su, Y. Multi-component oil–water two phase flow in quartz and kerogen nanopores: A molecular dynamics study. *Fuel* **2024**, *362*, 130869.

(54) Errington, J. R.; Shen, V. K. Direct evaluation of multicomponent phase equilibria using flat-histogram methods. *The Journal of chemical physics* **2005**, *123* (16), 164103.

(55) Shen, V. K.; Siderius, D. W. Elucidating the effects of adsorbent flexibility on fluid adsorption using simple models and flat-histogram sampling methods. *The Journal of chemical physics* **2014**, *140* (24), 244106.

(56) Siderius, D. W.; Shen, V. K. Use of the grand canonical transition-matrix Monte Carlo method to model gas adsorption in porous materials. *The Journal of Physical Chemistry C* **2013**, *117* (11), 5861-5872.

(57) Siderius, D. W.; Hatch, H. W.; Errington, J. R.; Shen, V. K. Comments on “Monte Carlo simulations for water adsorption in porous materials: Best practices and new insights. *AichE J* **2022**, *68* (8), e17686.

(58) Shen, V. K.; Errington, J. R. Determination of fluid-phase behavior using transition-matrix Monte Carlo: Binary Lennard-Jones mixtures. *The Journal of chemical physics* **2005**, *122* (6), 064508.

(59) Steele, W. A. The physical interaction of gases with crystalline solids: I. Gas-solid energies and properties of isolated adsorbed atoms. *Surface Science* **1973**, *36* (1), 317-352.

(60) Humphrey, W.; Dalke, A.; Schulten, K. VMD: visual molecular dynamics. *Journal of molecular*

graphics **1996**, *14* (1), 33-38.

(61) Martin, M. G.; Siepmann, J. I. Transferable potentials for phase equilibria. 1. United-atom description of n-alkanes. *The Journal of Physical Chemistry B* **1998**, *102* (14), 2569-2577.

(62) Potoff, J. J.; Siepmann, J. I. Vapor–liquid equilibria of mixtures containing alkanes, carbon dioxide, and nitrogen. *AIChE journal* **2001**, *47* (7), 1676-1682.

(63) Lorentz, H. A. Ueber die Anwendung des Satzes vom Virial in der kinetischen Theorie der Gase. *Annalen der physik* **1881**, *248* (1), 127-136.

(64) Frenkel, D.; Smit, B. *Understanding molecular simulation: from algorithms to applications*; Elsevier, 2023.

(65) Janeček, J. Long range corrections in inhomogeneous simulations. *The Journal of Physical Chemistry B* **2006**, *110* (12), 6264-6269.

(66) Yeh, I.-C.; Berkowitz, M. L. Ewald summation for systems with slab geometry. *The Journal of chemical physics* **1999**, *111* (7), 3155-3162.

(67) Hatch, H. W.; Mittal, J.; Shen, V. K. Computational study of trimer self-assembly and fluid phase behavior. *The Journal of Chemical Physics* **2015**, *142* (16), 164901.

(68) Siepmann, J. I.; Frenkel, D. Configurational bias Monte Carlo: a new sampling scheme for flexible chains. *Molecular Physics* **1992**, *75* (1), 59-70.

(69) Vlugt, T.; Martin, M.; Smit, B.; Siepmann, J.; Krishna, R. Improving the efficiency of the configurational-bias Monte Carlo algorithm. *Molecular Physics* **1998**, *94* (4), 727-733.

(70) Martin, M. G.; Frischknecht, A. L. Using arbitrary trial distributions to improve intramolecular sampling in configurational-bias Monte Carlo. *Molecular Physics* **2006**, *104* (15), 2439-2456.

(71) Zimmermann, A. S.; Lirio, R.; Castro, B. M.; Romanielo, L.; Mattedi, S. How well can damped shifted force Monte Carlo predict vapor–liquid equilibria for natural gas systems? *Brazilian Journal of Chemical Engineering* **2024**, 1-11.

(72) Shen, V. K.; Errington, J. R. Metastability and instability in the Lennard-Jones fluid investigated by transition-matrix Monte Carlo. *The Journal of Physical Chemistry B* **2004**, *108* (51), 19595-19606.

(73) Clark, M. D.; Morris, K. R.; Tomassone, M. S. Correlation of solubility with the metastable limit of nucleation using gauge-cell monte carlo simulations. *Langmuir* **2017**, *33* (36), 9081-9090.

(74) Errington, J. R. Evaluating surface tension using grand-canonical transition-matrix Monte Carlo simulation and finite-size scaling. *Physical Review E* **2003**, *67* (1), 012102.

(75) Shen, V. K.; Errington, J. R. Determination of surface tension in binary mixtures using transition-matrix Monte Carlo. *The Journal of chemical physics* **2006**, *124* (2).

(76) Singh, J. K.; Kwak, S. K. Surface tension and

vapor-liquid phase coexistence of confined square-well fluid. *The Journal of chemical physics* **2007**, *126* (2), 024702.

(77) Cui, W.; Liang, Y.; Masuda, Y.; Tsuji, T.; Matsuoka, T.; Takahashi, H. Estimation of the minimum miscibility pressure for CO₂-crude-oil systems by molecular dynamics simulation. *Petroleum Research* **2023**, *8* (1), 1-10.

(78) Shi, J.; Tao, L.; Guo, Y.; He, X.; Li, Y.; Bao, B. Visualization of CO₂-oil vanishing interface to determine minimum miscibility pressure using microfluidics. *Fuel* **2024**, *362*, 130876.

(79) Fang, T.; Zhang, Y.; Liu, J.; Ding, B.; Yan, Y.; Zhang, J. Molecular insight into the miscible mechanism of CO₂/C₁₀ in bulk phase and nanoslits. *International Journal of Heat and Mass Transfer* **2019**, *141*, 643-650.